Research Square

Preprints are preliminary reports that have not undergone peer review.
They should not be considered conclusive, used to inform clinical practice,
or referenced by the media as validated information.

Correspondence Between Structural and Functional Connectivity Within White Matter

Sapna S Mishra
New Jersey Institute of Technology
Kartikeya Kulkarni
New Jersey Institute of Technology
Pratik Jain
New Jersey Institute of Technology
Paul A. Taylor
National Institute of Mental Health, NIH
Bharat Biswal
bbiswal@gmail.com

New Jersey Institute of Technology

Research Article

Keywords:

Posted Date: November 19th, 2026

DOI: https://doi.org/10.21203/rs.3.rs-11473390/v1

License: This work is licensed under a Creative Commons Attribution 4.0 International License.
Read Full License

Additional Declarations: No competing interests reported.

Correspondence Between Structural and Functional Connectivity Within White Matter

Sapna S Mishra[1,†], Kartikeya Kulkarni[1,†], Pratik Jain[1,2], Paul A. Taylor[3], Bharat Biswal[1*]

[1] New Jersey Institute of Technology, Newark, NJ, United States
[2] Rutgers School of Graduate Studies, Newark, NJ, United States
[3] Scientific and Statistical Computing Core, National Institute of Mental Health, NIH, Bethesda, MD, United States

†Shared authorship
*Corresponding Author: Bharat Biswal (bbiswal@gmail.com)

Abstract

White matter functional networks (WMFNs) derived from resting-state BOLD fluctuations have been identified across multiple datasets, but whether they correspond to coherent anatomical units defined by the underlying axonal architecture remains untested. Here we tested WM structural connectivity-functional connectivity (SC-FC) coupling directly by asking whether regions co-assigned to the same WMFN are preferentially linked by WM tracts. Using resting-state fMRI and diffusion MRI from the Human Connectome Project 7T dataset (N = 161), we derived 11 WMFNs per session (after exclusion of one boundary network) via k-means clustering of voxel-level functional connectivity (FC), constructed structural connectivity (SC) using multi-shell multi-tissue constrained spherical deconvolution with anatomically constrained tractography, and quantified the correlation between SC and FC across within- and between-network edges. Within-network coupling was two to three times higher than between-network coupling in both sessions (Session 1: $r_{within} = 0.59$ vs. $r_{between} = 0.20$; Session 2: $r_{within} = 0.66$ vs. $r_{between} = 0.28$; $p < 0.001$). The increased coupling was also observed across subjects, in terms of survived matching of edge counts, and disappeared when network labels were permuted. Network-level coupling was heterogeneous and concentrated in projection pathways spanning the midbrain and medulla oblongata, with rank ordering of the six highest-coupling networks identical across sessions. These findings provide structural support that WMFNs are coherent anatomical-functional units and support reconceptualising WM as a structured contributor to the brain's functional architecture rather than a passive transmission medium.

1. Introduction

The human brain's functional organisation has been mapped with considerable precision over the past two decades through resting-state functional MRI (rsfMRI), revealing that spontaneous fluctuations in the blood oxygen level-dependent (BOLD) signal co-vary across spatially distributed regions in reproducible, low-frequency patterns known as intrinsic functional networks (FNs) (Biswal et al., 1995). This body of work has transformed our understanding of how neural systems are organised and has established rsfMRI as an important tool in cognitive and clinical neuroscience (Biswal & Uddin, 2025). Yet, existing functional literature has limited its examination almost entirely to grey matter (GM) (Gore et al., 2025).

White matter (WM), which constitutes roughly half of total brain volume, has been systematically excluded from functional neuroimaging (Black, 2007) under the assumption that BOLD contrast, driven primarily by postsynaptic activity, is absent in myelinated fibres (Logothetis et al., 2001). This exclusion has been increasingly challenged along several lines of converging evidence (Grajauskas et al., 2019; Li

et al., 2025). Despite WM blood flow and volume being approximately one quarter of those in GM, the haemodynamic response remains detectable with modern acquisition sequences (Ding et al., 2025; Gore et al., 2019), and task-evoked BOLD changes have been demonstrated in tract-specific patterns: along the optic radiation during visual stimulation (Wang et al., 2023), in the corpus callosum during interhemispheric coordination (Gawryluk et al., 2011a) and in the internal capsule during motor tasks (Gawryluk et al., 2011b), with comparable activation reported during a cognitive processing-speed task (Gawryluk et al., 2014).

Further evidence for the functional organisation of WM has emerged from studies applying data-driven network-identification approaches directly to WM rsfMRI time series (Itkyal et al., 2025; Li et al., 2025; Peer et al., 2017). Peer and colleagues used *k*-means clustering of resting-state BOLD fluctuations to delineate distinct WM functional networks (WMFNs) that correspond spatially to established tract anatomy and functionally to canonical GM networks (Peer et al., 2017). Independent component analysis has identified WM patterns that reorganise during naturalistic stimulation (Marussich et al., 2017), and subsequent work has established the test-retest reliability of WM functional connectivity (WM-FC) and its sensitivity to individual differences (Wang et al., 2022). WM-FC patterns have also been shown to be disrupted in neurological and psychiatric conditions, including Alzheimer's disease (Das et al., 2025, Gao et al., 2020; Jiang et al., 2025) and major depressive disorder (Li et al., 2025), and undergo systematic maturational change across early development (Huang et al., 2024). Jain and colleagues introduced the WhiFuN toolbox for WM-FC analysis, which incorporates preprocessing designed to minimise GM signal contamination, together with optimised signal extraction and statistical tools (Jain et al., 2025).

While fMRI captures the functional dimension of WM organisation, diffusion MRI (dMRI) provides a structural perspective, mapping microstructural properties, fibre architecture, and large-scale structural connectivity (SC) with high spatial and angular precision (Jeurissen et al., 2014; Tournier, 2019). WM microstructure varies systematically across individuals and the lifespan, and these variations are predictive of cognitive performance, psychiatric vulnerability, and neurological outcomes (Kelly et al., 2018; Kinnunen et al., 2011; Penke et al., 2010). Through tractography-based connectomics, dMRI has further provided a structural basis for understanding the large-scale organisation of WM (Smith et al., 2012; Tournier, 2019).

In current literature, it remains largely unexplored is whether the structural and functional organisation in WM are coupled, that is, whether regions belonging to the same WMFN tend to exhibit greater SC than regions belonging to different networks (Li et al., 2024; Zhao et al., 2023). In GM, structural connectivity-functional connectivity (SC-FC) coupling has been observed at multiple spatial scales and is considered a marker of system-level integration (Fotiadis et al., 2024; Seguin et al., 2023). However, GM SC-FC coupling is inherently a cross-tissue relationship where the functional signal is sampled from cortical GM while the SC linking those regions runs through WM tracts. Coupling in this case reflects how one tissue type (WM) anatomically scaffolds signals measured in another (GM). WM SC-FC coupling, by contrast, is intrinsic to a single tissue where both the functional BOLD signal and the structural pathway originate within the same WM substrate, so any observed coupling reflects a more direct anatomical correspondence between the medium of conduction and the medium in which functional fluctuations are measured. If analogous coupling does exist within WM, it would provide independent structural validation that WMFNs represent coherent anatomical-functional units, rather than statistical summaries of BOLD covariance (Wang et al., 2021; Zhao et al., 2023).

The convergence of WM-fMRI-based findings across methodologies, cohorts, and clinical contexts provides substantive support for the position that WM rsfMRI yields biologically meaningful variation in neural function, rather than constituting residual physiological noise (Ding et al., 2025; Li et al., 2025; Nelson et al., 2026). What remains unestablished, however, is whether WMFNs derived from BOLD covariance are anchored to the brain's underlying axonal architecture, or whether their organisation is de-

fined solely in the functional domain. In this study, we hypothesised that regions co-assigned to the same WMFN are preferentially linked by WM tracts, such that within-network SC-FC coupling systematically exceeds between-network SC-FC coupling. We tested this hypothesis using high-resolution resting-state fMRI and diffusion MRI from the Human Connectome Project (HCP) 7T dataset, evaluating both the reproducibility of the within-network advantage across independent scan sessions and the capacity of ultra-high-field imaging to resolve WM SC-FC coupling with high spatial specificity. This study provides first direct within- vs between-network contrast of WM SC-FC coupling, at 7T, with a fully held-out replication.

2. Methods

2.1 Participants and Datasets

Data were drawn from the Young Adult release of the HCP (Van Essen et al., 2013). All HCP data were acquired under institutional review board approval at Washington University in St. Louis, and all participants provided written informed consent prior to participation, including consent to share de-identified data. The present study constitutes secondary analysis of pre-existing, de-identified data and did not require additional institutional ethical review.

The analytical sample was derived from the HCP 7T dataset, which scanned a subset of HCP participants on a Siemens Magnetom 7T scanner to acquire high-resolution structural, functional, and diffusion MRI. A total of 166 participants had complete resting-state fMRI data across both 7T scan sessions (acquired on separate days) alongside a complete 7T diffusion MRI acquisition (age range: 22–36 years; 102 females). Session 2 resting-state fMRI data were designated as an independent replication sample and remained unanalysed until all analytical pipelines for Session 1 were finalised.

2.2 MRI Data Acquisition

T1-weighted structural images were acquired using a 3D MPRAGE sequence (repetition time [TR] = 2,400 ms, echo time [TE] = 2.14 ms, 0.7 mm isotropic voxels). RsfMRI data were acquired using a multiband gradient-echo EPI sequence (TR = 1,000 ms, TE = 22.2 ms, 1.6 mm isotropic voxels, multiband acceleration factor = 5), with two 15-minute runs acquired per session across two separate days (four runs total). dMRI was acquired using a spin-echo EPI sequence at 1.05 mm isotropic spatial resolution across two b-value shells (b = 1,000 and 2,000 s/mm²) with 65 diffusion-encoding directions per shell.

2.3 MRI Preprocessing

Both rsfMRI and dMRI data were obtained as HCP minimally preprocessed outputs (Glasser et al., 2013), which include motion correction, EPI distortion correction, registration to T1-weighted space, and nonlinear normalisation to MNI-152 standard space. RsfMRI data were further denoised using ICA-FIX to remove motion and physiological artefacts (Salimi-Khorshidi et al., 2014; Griffanti et al., 2014). Tissue segmentation was performed on the T1-weighted image to delineate GM, WM, and CSF using FSL FAST (FMRIB's Automated Segmentation Tool, FSL v6.0). The dMRI outputs additionally include eddy-current and gradient nonlinearity correction. The minimally preprocessed dMRI data was then additionally denoised using the "*dwidenoise*" command in MRtrix3 (Tournier et al., 2019), which implements Marchenko-Pastur principal component analysis (Veraart et al., 2016) to improve signal-to-noise ratio while preserving underlying diffusion signal.

2.4 ROI definition: White Matter Functional Networks

WMFNs serve as the common parcellation framework across both fMRI and dMRI. Using the WhiFuN toolbox (Jain et al., 2025), 12 WMFNs were defined separately for each session of the HCP 7T dataset (k=12). Clustering was run independently on Session 1 and Session 2 functional datasets rather than forcing Session 2 onto Session 1's spatial boundaries. Each WMFN was identified by applying k-means clustering to the group-averaged voxel-level WM rs-FC matrix, partitioning WM voxels into spatially coherent networks based on functional signal similarity. The optimal number of networks (k) was determined via the cluster stability criterion implemented in WhiFuN. For each session, one WMFN was excluded due to its location at the GM/WM boundary because of its increased susceptibility to partial-volume artifacts. The remaining 11 WMFNs per session then served as the framework for both fMRI and dMRI analyses.

Because k-means clustering groups voxels strictly by temporal signal similarity, individual WMFNs consisted of spatially discontinuous 3D connected components. To construct discrete node region-of-interest (ROI) targets for SC and FC matrices, contiguous 3D spatial clusters were extracted from each network. Bilateral clusters spanning both hemispheres (e.g., within the corpus callosum and brainstem) were bisected along the MNI sagittal midline to create distinct left and right hemispheric ROIs. Excluding small, noisy fragments containing fewer than 20 voxels resulted in a total of 34 node ROIs for Session 1 and 40 node ROIs for Session 2. Since node extraction was performed on session-native clusters, the two sessions comprise distinct node and edge sets; consequently, Session 2 evaluates the replication of the network-level organizational contrast (within- vs. between-network coupling) rather than an edge-for-edge comparison of identical connectivity pairs.

To evaluate network-specific properties consistently across sessions while preserving session-native cluster boundaries, spatial correspondence between the networks of the two sessions was verified. 8 out of the 11 networks demonstrated high spatial congruence across sessions and were directly assigned the numerical identifiers of their Session 1 counterparts. The remaining 3 networks (WMFN1,WMFN2, and WMFN8) were assigned identifiers based on maximal relative spatial overlap. The WM networks for Session 1 are shown in Fig.1, and those for Session 2 are depicted in Fig. S1.

All node ROIs were defined in MNI standard space and inverse-warped into each participant's native diffusion space in order to run subsequent tractography analysis (below). Visual quality control of the transformed atlases identified registration errors in 5 participants which were then excluded from further analysis, yielding a final analytical sample of $N = 161$ across both sessions.

2.5 Tractography

Fibre orientation distributions (FODs) were estimated in each voxel within each participant's native diffusion space using multi-shell, multi-tissue constrained spherical deconvolution (Jeurissen et al., 2014) in MRtrix3 (Tournier et al., 2019). Tissue response functions were estimated for WM, GM, and CSF, and the resulting WM FOD image was used to drive tractography. Whole-brain probabilistic tractography was generated using the second-order integration over fibre orientation distributions (iFOD2) algorithm with a dynamic seeding strategy within the WM FOD. A total of 10 million streamlines were generated using an FOD amplitude cutoff of 0.06, with minimum and maximum streamline lengths of 10 mm and 250 mm, respectively. The iFOD2 algorithm mitigates overshooting in sharply curved pathways and traverses complex crossing-fibre architecture, which is critical in regions such as the corona radiata and centrum semiovale. Anatomically constrained tractography (ACT; Smith et al., 2012) was applied using a five-tissue-type (5TT) segmentation image derived from the T1-weighted structural image to guide streamline propagation and termination. Structural connectomes were constructed using MRtrix3's "*tck2connectome"* command, assigning whole-brain streamlines to the inverse-warped, subject-native ROI atlas to generate pairwise ROI-to-ROI connectivity matrices. For each connection, the streamline

count was extracted, along with the mean fractional anisotropy (FA) averaged over the connecting streamlines.

2.6 Characterising Functional and Structural Connectivity

FC was derived by computing pairwise Pearson correlations between average rsfMRI time series across all ROI pairs, yielding subject-specific FC matrices that quantified the temporal coherence of WM rsfMRI signals across the ROIs. All FC values were Fisher z-transformed to stabilise variance and expressed as absolute values, such that coupling estimates reflected the strength of functional synchronisation.

In parallel, SC was derived from tractography-based connectomes of each subject, and mean FA and streamline count were extracted for every ROI pair. These two measures were integrated into a single composite edge-weight (*EW*), defined as

$$EW = FA \times streamline\ count^{\gamma}$$

jointly capturing the microstructural integrity of each WM tract and the robustness of its interregional connections. The exponent γ was introduced as a scaling parameter to prevent streamline count from disproportionately dominating the composite at the expense of FA. Following Betzel et al. (Betzel et al., 2014), γ was set to 0.6, a value that sufficiently compresses the streamline count distribution so that both measures contribute meaningfully to the composite. This scaling mitigates the size-dependent bias inherent in raw streamline counts, ensuring that large tracts do not overshadow the contribution of smaller WM connections. Pairwise ROIs with zero connecting streamlines were retained in the SC matrices with an assigned edge weight of zero, representing a negligible proportion of overall matrix edges (Session 1: $0.37\% \pm 0.29\%$). This composite EW served as the primary index of SC strength throughout all subsequent analyses.

2.7 Structure-Function Coupling Analysis and Statistical Testing

With structural and functional matrices defined over a common parcellation, the degree of correspondence between them was systematically quantified at the subject, group, and network levels. Tractography-based connectome construction yielded a symmetric $M \times M$ SC matrix per participant, where M denotes the number of ROIs. FC matrices of equivalent dimensions were derived as described in Section 2.6. Unique pairwise edges were recovered from the upper-triangular portion of each matrix, excluding the diagonal.

Edges were classified as *within-network connections* when both ROIs belonged to the same WMFN, and as *between-network connections* when they spanned different networks. This partitioned all $M(M-1)/2$ unique ROI pairs per dataset (561 and 780 pairs for the two sessions, respectively) into within- and between-network classes, yielding 49 within-network and 512 between-network pairs for the Session 1 dataset, and 73 within-network and 707 between-network pairs for the Session 2 dataset.

Subject-Level Coupling. For each participant, edges were separated into paired SC and FC vectors for within-network and between-network classes, and Pearson correlations were computed to yield subject-specific coupling coefficients (r_{within} and r_{between}). Correlation coefficients were Fisher z-transformed to normalize sampling distributions prior to parametric testing. To test whether SC-FC coupling was significantly stronger within WMFNs than between them, a two-tailed paired-samples t-test was applied across subject-wise Fisher z-transformed values, with Cohen's d_z computed for effect size.

To confirm that differences between connection classes were driven by true WMFN topology, two control procedures were implemented in Session 1:

(a) Edge-Count Matching: Within- and between-network edge vectors were randomly subsampled to equal lengths of l=35 edges over 100 repetitions per participant, and coupling differences were re-evaluated across averaged equalized vector sizes. 35 edges were chosen as a conservative subsampling threshold below the 49 total within-network edges.
(b) Label-Permutation Null Model: ROI-to-network assignments were randomly permuted 100 times while preserving original network sizes and cluster counts. Coupling analyses were repeated on the randomized network assignments to confirm that the within-network advantage is significantly attenuated when functional topology is disrupted.

Group-Level Coupling. To provide a descriptive consensus characterization of SC-FC coupling, group-averaged SC and FC matrices were constructed. Subject-wise FA and streamline count matrices were averaged across all participants to yield group-mean structural matrices, from which edge weights were computed. FC matrices were averaged across subjects in the same manner. Upper-triangular edge values were extracted, stratified into within- and between-network classes, and correlated using Pearson's r to yield group-level coupling coefficients (r_{group}). Group-mean matrices serve as noise-reduced topological representations that complement the primary subject-level analyses.

Network-Level Coupling. A network-level SC-FC coupling score ($r_{network}$) was computed for each subject and network to evaluate functional heterogeneity across individual WMFNs. For each participant and network k, the SC and FC values of each constituent within-network edge were z-scored relative to that participant's whole-brain edge distribution, and the coupling score was taken as the mean of their element-wise product. Standardizing edge weights relative to the whole-brain baseline prior to taking the element-wise product preserves local alignment while accounting for differences in network size.

3. Results

3.1 White Matter Functional Networks

Group-level k-means clustering applied to WM rsfMRI matrices identified spatially distinct WMFNs across both scan sessions. This yielded 11 valid networks in each of HCP 7T Session 1 and Session 2. The spatial topography of each network is illustrated in Fig. 1 for Session 1 and Fig. S1 for Session 2, with corresponding anatomical regions summarized in Table 1. Cross-session spatial overlap analyses confirmed high spatial reproducibility between independent session clustering, achieving a mean cross-session dice similarity coefficient (DSC) of $\mathbf{0.785 \pm 0.135}$ (median: $\mathbf{0.860}$, range: $\mathbf{0.535 - 0.896}$). Specifically, 8 of the 11 networks exhibited strong spatial reproducibility with DSC $> \mathbf{0.80}$, while the remaining 3 networks demonstrated moderate overlap (DSC $= \mathbf{0.535 - 0.603}$). Topographically, these reproducible networks mapped onto primary white matter pathways, including the corpus callosum, superior longitudinal fasciculus, corticospinal tract, cingulum, and inferior fronto-occipital fasciculus. Replicability and measurement reliability analysis of WMFNs is presented in the Supplementary Material provided with this manuscript.

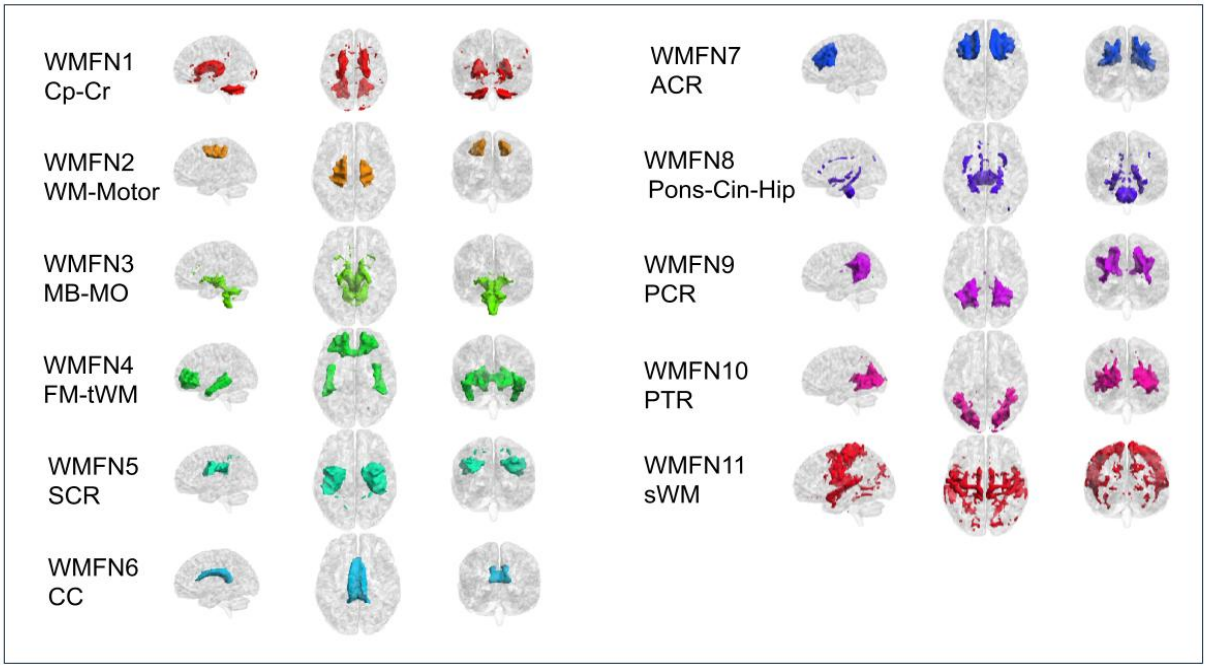


Figure 1. Spatial topography of 11 white matter functional networks (WMFNs) identified in the HCP 7T session 1 dataset. The WMFNs were derived by applying *k*-means clustering to the group-averaged voxel-level WM resting-state functional connectivity matrix using the WhiFuN toolbox (Jain et al., 2025), with the number of clusters selected based on cluster stability. Keys: WM: White Matter, Cp-Cr: Capsule-Cerebellum, MB-MO: Midbrain and Medulla Oblongata, FM-tWM: Forceps Minor and Temporal WM, SCR: Superior Corona Radiata, CC: Corpus Callosum, ACR: Anterior Corona Radiata, Cin-Hip: Cingulum Hippocampus, PCR: Posterior Corona Radiata, PTR: Posterior Thalamic Radiation, sWM: Superficial WM.

Table 1. Regions corresponding to white matter functional networks of HCP 7T Session 1 dataset.

White Matter Functional Networks	**White Matter Regions**
WMFN1	Capsule-Cerebellum
WMFN2	White Matter Motor
WMFN3	Midbrain and Medulla Oblongata
WMFN4	Forceps Minor and Temporal WM
WMFN5	Superior Corona Radiata
WMFN6	Corpus Callosum
WMFN7	Anterior Corona Radiata
WMFN8	Pons and Cingulum Hippocampus
WMFN9	Posterior Corona Radiata
WMFN10	Posterior Thalamic Radiation
WMFN11	Superficial White Matter

3.2 Stronger Structure-Function Coupling Within White Matter Functional Networks

Subject-Level Coupling Across Datasets

Systematic quantification in the HCP 7T Session 1 dataset revealed that structural and functional architectures are coupled significantly more tightly within WMFN boundaries ($r_{within} \approx 0.59$) than across them ($r_{between} \approx 0.20$; t (160) = 47.12, $p < 0.001$, d_z=3.71). This within-network coupling advantage was consistent across almost all participants, with paired slope plots illustrating a near-universal drop in coupling as connections cross network boundaries (Fig. 2A).

This pattern was replicated in Session 2 data as well, where within-network coupling was significantly higher ($r_{within} \approx 0.66$) relative to between-network coupling ($r_{between} \approx 0.28$; t (160) = 52.70, $p<0.001$, d_z =4.15). The paired slope analysis demonstrated the same near-universal attenuation across network boundaries (Fig. 2B). Statistical results for all subject-level paired comparisons across datasets are summarized in Table 2.

Sensitivity and Topological Control Analyses

Control analyses in the HCP 7T Session 1 dataset confirmed that elevated within-network coupling was topological and not an artifact of edge-count disparities or vector length differences. As depicted in Fig. 3, subsampling within- and between-network edge vectors to an equal length of 35 edges across 100 repetitions yielded a virtually identical coupling advantage (mean difference of Pearson's correlation = 0.3851), with $r_{within} > r_{between}$ in 100% of repetitions. Furthermore, randomly permuting ROI network assignments while preserving original network sizes eliminated the within-network advantage (mean difference of Pearson's correlation = −0.0632; Fig. 4), confirming that elevated SC-FC coupling explicitly requires intact WMFN architecture.

Group-Level Consensus Coupling

At the group level, SC and FC were strongly correlated across within-network edges in the Session 1 dataset (r_{group}=0.655, $p<0.001$), whereas this relationship was markedly attenuated for between-network edges (r_{group}=0.225, $p<0.001$; Fig. 5a). This consensus pattern was maintained in the Session 2 data (r_{group}=0.758, $p<0.001$ for within-network vs. r_{group}=0.389, $p<0.001$ for between-network edges; Fig. 5b).

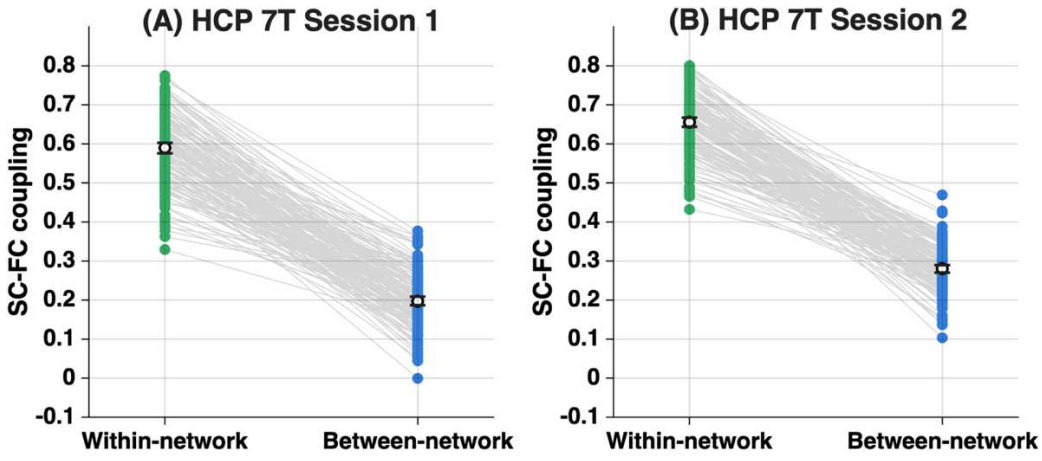


Figure 2. Subject-level SC-FC coupling coefficients for within-network (green) and between-network (blue) connections displayed as paired slope plots for (a) HCP 7T Session 1 and (b) Session 2. Each line connects the within-network and between-network coupling coefficients of a single participant, with the open circle and error bars denoting the group mean ± 95% confidence interval. Across all participants and all datasets, within-network coupling was higher than between-network coupling.

Table 2. Summary of the primary statistical results across two scan sessions. The within-network advantage in SC-FC coupling was robust across imaging sessions, providing strong converging evidence for the organisational coherence of WMFNs.

Dataset	**Mean r_{within}**	**Mean $r_{between}$**	**Mean difference (in correlation values)**	***t* (df)**	***Cohen's d_z***
HCP 7T Session 1	0.5896	0.1978	0.3918	$t(160) = 47.12$	3.71
HCP 7T Session 2	0.6560	0.2801	0.3759	$t(160) = 52.70$	4.15

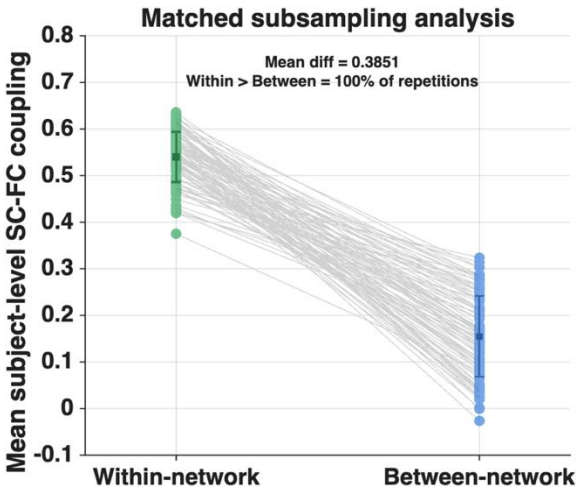


Figure 3. Subject-level SC-FC coupling for within-network (green) and between-network (blue) connections in the HCP 7T Session 1 dataset after equalizing edge counts (l=35, 100 repetitions; N=161). Error bars show the group means ± 95% CI. Within-network coupling exceeded between-network coupling across 100% of repetitions (mean difference = 0.3851).

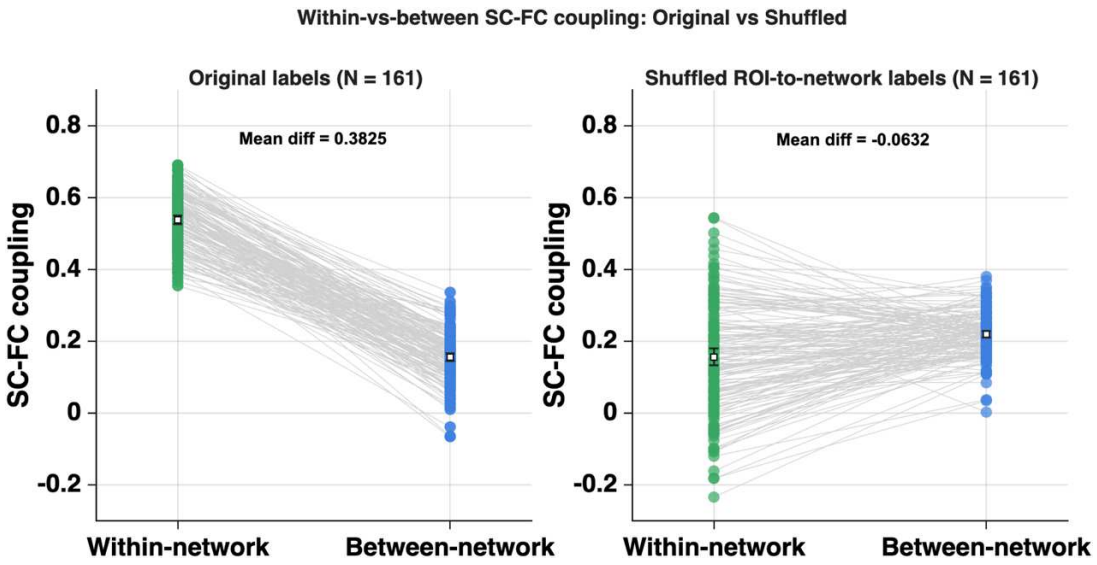


Figure 4. Subject-level SC–FC coupling under original (left) versus permuted (right) ROI-to-network assignments across 100 randomizations in the Session 1 dataset. Error bars indicate group mean ±95% CI. Shuffling network labels eliminated the within-network advantage (mean difference dropped from 0.3825 to −0.0632), demonstrating that coupling depends strictly on intact network architecture.

3.3 Network-Specific Coupling Patterns

Network-level SC-FC coupling ($r_{network}$) was computed for each participant and network as the mean product of z-scored SC and FC values across within-network edges, normalized relative to each subject's whole-brain edge distribution. The resulting scores quantify the degree to which within-network edges co-deviate above the whole-brain baseline. Ranking networks by mean $r_{network}$ across participants revealed marked heterogeneity in structure-function alignment across individual WMFNs (Fig. 6). Rank ordering was highly reproducible across both HCP 7T sessions. The top six networks occupied identical rank positions in both sessions, with remaining five having negligible coupling across the sessions. In both sessions, WMFN3 (corresponding to midbrain and medulla oblongata projection tracts) ranked first by a substantial margin $r_{network}$ 25.7 in Session 1; $r_{network}$ 21.8 in Session 2), whereas all other networks recorded mean scores below 5.0. Positive coupling was also observed in WMFN10, WMFN7, WMFN9, WMFN4, and WMFN11. Conversely, several networks (including WMFN2 and WMFN5 in Session 1) exhibited mean scores near or below zero, indicating no systematic co-elevation of SC and FC above whole-brain baseline. Network-level SC-FC coupling is thus heavily concentrated in a single projection-centred network, with remaining functional networks contributing minimally to baseline-exceeding coupling.

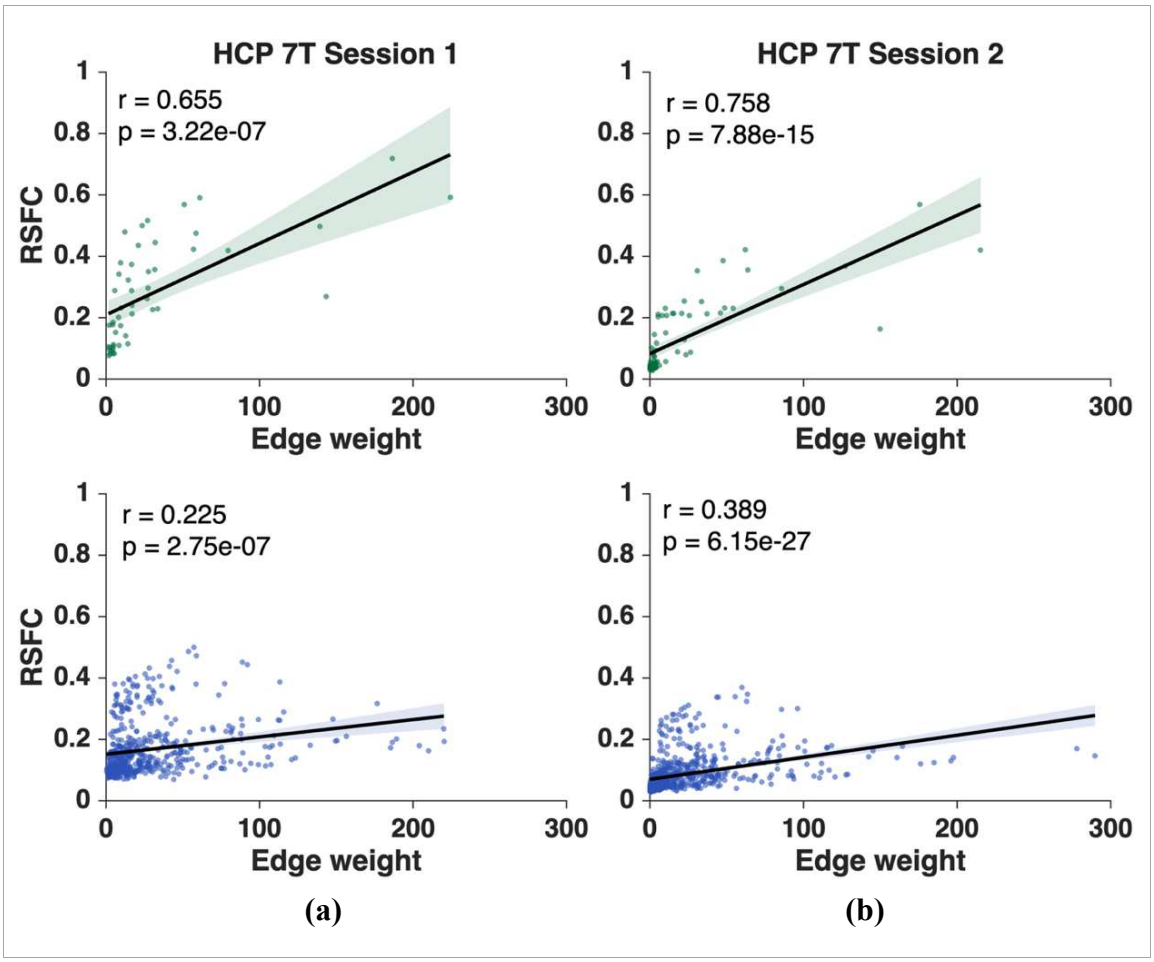


Figure 5. Group-level scatter plots illustrating SC-FC coupling for within-network (top row) and between-network (bottom row) connections across the two scans. In HCP 7T session 1, (a) within-network connections again showed a strong positive association (r_{group}=0.655, p<0.001), while between-network connections exhibited a weaker relationship (r_{group}=0.225, p<0.001). In HCP 7T session 2 (b), within-network connections showed a strong positive association (r_{group} = 0.758, p < 0.001), whereas between-network connections showed a weaker relationship (r_{group} = 0.389, p < 0.001). Each point corresponds to a unique ROI pair, and the black line represents the linear regression fit.

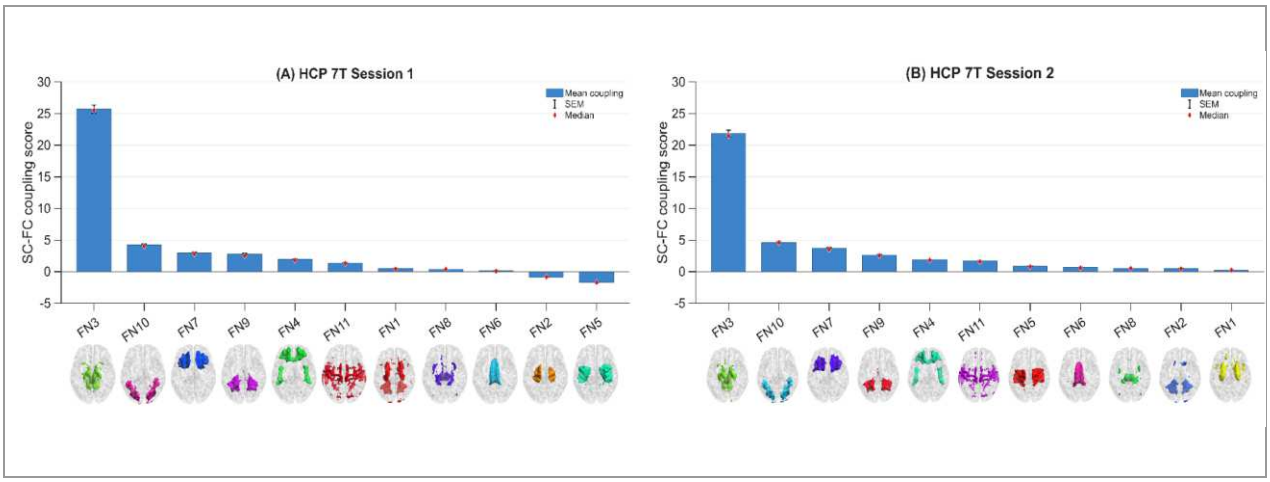


Figure 6. Network-level SC-FC coupling scores ($r_{network}$) across white matter functional networks (WMFNs) in the HCP 7T (a) session 1 and (b) session 2 datasets. Bars represent group-mean coupling scores (mean ± standard error of mean [SEM]), ranked in descending order; red diamonds indicate network medians. Coupling was calculated as the mean element-wise product of *z*-scored SC and FC edge values within each network, normalised to each subject's whole-brain connectivity distribution. WMFN3 (midbrain and medulla oblongata) showed substantially higher coupling than all other networks, followed by posterior thalamic radiation and a drop across the remaining networks.

4. Discussion

4.1 Significant Coupling Between Structural and Functional Connectivity in White Matter

Our study demonstrates that SC and FC in WM are significantly coupled: within-network coupling was two- to three-times that of between-network coupling across two independent scan sessions in a large ultra-high-field 7T cohort (N=161). This pattern was replicated with high consistency across independent scan sessions. These findings provide structural evidence that WMFNs identified through data-driven clustering of rsfMRI time series correspond to interconnected anatomical units defined by the underlying axonal architecture.

In GM, SC-FC coupling varies along a sensory-association hierarchy (Fotiadis et al., 2024; Vázquez-Rodríguez et al., 2019). Our findings extend this principle into WM, demonstrating that functional co-activation preferentially aligns with structural connectomes. Network-level analyses revealed substantial heterogeneity among WMFNs, with coupling strength ($r_{network}$) ranging from near-zero in certain networks to markedly elevated values in others. Specifically, projection pathways spanning the midbrain and medulla oblongata (WMFN3) exhibited coupling scores of $r_{network}$ 25.7 in Session 1 and 21.8 in Session 2, more than five-fold higher than all other networks (25.7 vs < 5.0). Across both sessions, the posterior thalamic radiation (WMFN10) and anterior corona radiata (WMFN7), alongside the posterior corona radiata (WMFN9) in Session 1, also demonstrated high network-level coupling. These pathways represent some of the most orientationally coherent structures in the brain, where uniform parallel fibre organization preserves voxel-level FA and supports robust streamline reconstruction, together maximizing both terms of our composite *EW*.

Conversely, networks overlapping regions of high fibre complexity scored near zero, including the superior corona radiata (WMFN5) and the WM motor network (WMFN2) in Session 1. In these regions, crossing, kissing, and fanning fibre configurations induce dMRI voxel-averaging artifacts that reduce FA and impede streamline propagation (Jeurissen et al., 2013). Because our SC metric relies on the product of FA and streamline count, these local tractography limitations systematically depress measured SC, which may lower $r_{network}$ values independently of underlying functional coupling. The tract-specific coupling profiles observed here therefore reflect both biological variation in structure-function alignment and methodological constraints inherent to diffusion-based tractography in complex WM architecture.

4.2 Mechanistic Basis: From Microstructure to Macroscale Coupling

The observation that diffusion-derived SC correlates with the magnitude of FC between WM regions raises fundamental questions about the mechanistic link between microstructural properties and functional dynamics. While the present study does not resolve these mechanisms directly, the findings are most consistent with models in which WM rsfMRI signals reflect metabolic activity coupled with axonal conduction and glial support processes, rather than vasculature or GM contamination. Two lines of evidence support this interpretation. First, the spatial specificity of SC-FC coupling argues against a purely vascular confound. If WM rsfMRI signals were driven primarily by systemic vascular effects, such as shared drainage through periventricular medullary veins (Özbay et al., 2018), then FC patterns should reflect

vascular territory topology rather than axonal connectivity. The observed alignment with tractography-defined structural networks instead suggests that the haemodynamic response is spatially organised according to the underlying fibre scaffold. While certain microvascular beds may partially run parallel to local tract paths, a generic vascular confound would induce uniform regional co-activation across adjacent tissue. Instead, our findings demonstrate edge-specific coupling that scales quantitatively with tract-specific properties, a relationship that disappears entirely when network topologies are shuffled. Second, the tract-specific heterogeneity in coupling strength is consistent with evidence that WM microstructural properties shape structure-function relationships at the network level (Nelson et al., 2026; Zhao et al., 2023), paralleling the role of intracortical myelination in cortical coupling (Fotiadis et al., 2023). In our data, the strongest alignment occurred in coherently organised projection pathways, which is what would be expected of substrates that simultaneously maximise BOLD orientation specificity, since WM BOLD correlations follow local fibre geometry (Ding et al., 2018; Schilling et al., 2019), and tractography fidelity, which degrades in regions of crossing, kissing or fanning fibres (Jeurissen et al., 2013).

The metabolic basis of WM BOLD signals has been increasingly clarified in human imaging. Simultaneous FDG-PET/fMRI in healthy adults has shown that WM-FC and the amplitude of low-frequency BOLD fluctuations are spatially correlated with local glucose uptake (Guo et al., 2022; Zhou et al., 2023), establishing that WM BOLD reflects regional aerobic metabolism rather than vascular noise. Additional evidence from intracranial stereo-EEG in human patients has further shown that WM BOLD-FC corresponds to electrophysiological synchronisation across multiple frequency bands and aligns with diffusion-derived SC (Huang et al., 2023). Together, these findings implicate coordinated axonal activity, rather than vascular or partial-volume artifact, as the source of WM BOLD fluctuations. Unlike GM, where BOLD contrast is dominated by postsynaptic metabolic demand (Logothetis et al., 2001), WM contains comparatively few synapses, and its metabolic budget is instead dominated by the ionic fluxes associated with action potential propagation and by glial support of axonal energy needs through glucose import and lactate shuttling (Harris & Attwell, 2012; Saab et al., 2016; Looser et al., 2024).

Myelin itself appears to play a direct role in shaping macroscale coupling (Nelson et al., 2026). Fotiadis et al. (2023) showed that the spatial distribution of intracortical myelination, together with the balance of excitatory and inhibitory neurotransmitter systems, jointly shapes SC-FC coupling strength across cortical regions. These findings suggest that WM microstructural properties, captured here through composite diffusion metrics combining FA and streamline count, constrain functional dynamics not merely by providing anatomical pathways for signal transmission but by modulating conduction velocity, temporal synchronisation, and metabolic efficiency. The coupling we observe between diffusion-derived SC and BOLD-derived FC therefore reflects an integrative relationship in which microstructure shapes the spatiotemporal dynamics of coordinated activation across WMFNs.

It is important to acknowledge that structure does not determine function in a strict sense. Even in cortical networks, where the structure-function relationship has been studied extensively, FC is observed between regions lacking direct structural connections, mediated by polysynaptic pathways and shaped by local circuit dynamics (Preti & Van De Ville, 2019). The present findings demonstrate that structure constrains functional coupling within WM, but this constraint is probabilistic rather than deterministic. The residual variance in FC not explained by SC indicates that other factors, including regional differences in haemodynamic response latency (Li et al., 2019), task-dependent modulation of WM functional engagement (Schilling et al., 2023), and indirect polysynaptic communication through GM relays, also contribute to the observed patterns of FC in WM.

4.3 Implications for White Matter fMRI Research

The demonstration of robust SC-FC coupling in WM carries significant implications for theoretical models of brain network organization and practical methodological decisions in rs-FC research. The traditional GM-centric view, in which cortical and subcortical regions act as primary functional nodes while WM tracts serve merely as passive signal conduits, is increasingly recognized as incomplete (Li et al., 2024; Zu et al., 2024). Our findings strengthen an emerging alternative framework in which WM is conceptualized as an active participant in the brain's functional architecture, governed by intrinsic dynamics that actively contribute to and constrain large-scale network communication.

These results also carry direct methodological consequences for fMRI preprocessing pipelines. The routine practice of regressing out the mean WM signal as a nuisance covariate rests on the assumption that WM fluctuations are uninformative noise, an assumption directly challenged by the systematic alignment of WM-FC with structural architecture demonstrated across both 7T scan sessions. While nuisance regression serves a legitimate role in mitigating shared physiological noise, treating the entire WM signal as monolithic noise risks discarding neurobiologically meaningful signals. More nuanced denoising strategies that preserve local WM variation while eliminating global systemic artifacts are required to balance noise suppression with information preservation (Grajauskas et al., 2019).

Furthermore, our findings inform the ongoing development of whole brain connectome frameworks that integrate GM and WM signal dynamics. Li and colleagues (2024) recently introduced a WM engagement metric quantifying how WM-FC mediates GM-to-GM communication, showing that WM engagement varies across cognitive states and predicts individual task performance. Similarly, Zu and colleagues (2024) proposed a "triple-wise" correlational framework incorporating WM fMRI as a functional mediator between cortical regions, demonstrating that including WM signals enhances the predictive power of FC models. Both approaches implicitly assume that WM functional signals are spatially structured and biologically grounded, a premise directly validated by our SC-FC coupling results. As these integrative frameworks gain traction, demonstrating that WMFNs are anchored to coherent structural substrates provides essential empirical justification for treating WM as an active, constituent component of the human connectome.

4.4 Limitations and Future Directions

Several limitations of the present study warrant acknowledgment and suggest key directions for future investigation. The diffusion metrics employed to construct SC matrices rely on FA and streamline counts, which act as composite measures reflecting a mixture of underlying microstructural properties, including myelination density, axonal diameter, fibre coherence, and extracellular water content. While the multi-shell, high-angular-resolution diffusion protocol of the HCP 7T dataset enables advanced biophysical modelling, to maintain comparability with established literature our primary analyses utilized FA, a tensor-derived scalar that falls in orientationally heterogeneous voxels even where the underlying fibre populations are intact. Future research should leverage biophysically informed microstructural models, such as Neurite Orientation Dispersion and Density Imaging (NODDI) or diffusion kurtosis imaging (DKI), to evaluate whether specific microstructural parameters (e.g., neurite density vs. orientation dispersion) exhibit distinct, parameter-specific relationships with WM-FC.

In addition, two key methodological constraints related to FC magnitudes and structural tractography must be noted. FC matrices were constructed using absolute correlation values to capture overall coupling magnitude. While taking absolute values isolates the strength of signal co-variation, positive and negative BOLD correlations reflect distinct neurophysiological and vascular processes. Future studies should explicitly evaluate whether positive and negative WM-FCs display differential alignment with underlying structural pathways.

Second, SC was quantified using probabilistic streamline tractography. Reconstructed streamlines should be interpreted as algorithmic estimates of pathway traversal probability rather than direct quantitative measures of biological axonal density or connection strength. Streamline reconstruction remains highly sensitive to parameter choices, data noise, and false-positive connections. Furthermore, tractography algorithms exhibit systematic geometric biases, favouring short, straight pathways over long or sharply curved tracts due to distance decay and angular constraints. This geometric bias may have inflated apparent coupling in short, orientationally coherent projection pathways (such as WMFN3) while depressing observed coupling in longer, curved association fibres.

Although our findings demonstrate strong alignment between tract anatomy and functional connectivity, they cannot entirely rule out vascular contributions to WM rsfMRI signals. Resolving whether WM functional networks reflect neuroaxonal metabolic demand rather than shared vascular drainage warrants future investigation integrating detailed angioarchitecture maps. In particular, mesoscale in vivo vascular imaging, such as high-resolution whole-brain venous mapping (Gulban et al., 2026), offers a promising avenue to directly dissociate microvascular flow architecture from underlying tract-specific functional connectivity.

Finally, the translational and clinical utility of WM SC-FC coupling remains to be established. Extending this high-resolution 7T framework to clinical cohorts characterized by WM pathology could test whether structure-function decoupling serves as an early, sensitive biomarker of demyelination, axonal degeneration, or neuroinflammation. Longitudinal study designs will be essential to determine whether alterations in structure-function alignment precede or follow macroscale structural damage, and whether the restoration of coupling predicts functional recovery.

4.5 Conclusion

This study demonstrates that SC-FC coupling in WM is substantially stronger within FN boundaries than between them, a result that held across two resting-state acquisitions collected on separate days in the same participants and that survived controls for edge count and network topology. Coupling was heterogeneous across networks and concentrated in orientationally coherent projection pathways, a pattern that reflects both biological variation in structure-function alignment and the reduced sensitivity of tensor-derived structural measures in regions of complex fibre architecture. Taken together, these results provide structural evidence that WMFNs are anchored to the brain's axonal organisation rather than existing only as statistical summaries of BOLD covariance, and they strengthen the case for integrating WM into whole-brain models of functional architecture. They also carry a practical implication, since a WM signal that aligns systematically with tract anatomy is not well described as nuisance variance to be regressed away. What remains open is the mechanism. Establishing how microstructural properties shape the temporal dynamics of WM functional coupling, and whether decoupling tracks the onset of WM pathology, will determine how far this framework extends beyond the healthy young adult brain.

Data Availability Statement

Primary neuroimaging data analyzed in this study were provided by the Human Connectome Project (HCP) Young Adult 7T dataset (WU-Minn Consortium) and are publicly accessible via ConnectomeDB (https://db.humanconnectome.org/) upon agreeing to the HCP Open Access Data Use Terms. All analysis workflows were carried out using open-source neuroimaging software, including MRtrix3 (https://www.mrtrix.org/), FSL (https://fsl.fmrib.ox.ac.uk/fsl/), and WhiFuN toolbox (https://github.com/Brain-Connectivity-Lab/WhiFuN). The custom analysis and processing scripts used to generate the findings are publicly available at https://anonymous.4open.science/r/White-Matter-SCFC-7T-53EE.

Author Contributions

S.S.M. and **K.K.** contributed equally to this work as co-first authors. **S.S.M.** led the investigation, study design, and SC-FC coupling analyses. **K.K.** performed fMRI and dMRI data curation and processing, and co-conducted the SC-FC coupling analyses. **S.S.M.** and **K.K.** wrote the original manuscript draft. **P.J.** implemented the WMFN parcellation pipeline via WhiFuN and conducted cross-session spatial reproducibility analyses. **P.A.T.** contributed to formal analysis, and method verification. **B.B.** helped formulate the problem, provided resources, and supervised the study. All authors contributed to manuscript revision, read, and approved the final submission.

Acknowledgements

We thank Dr. Xin Di for his valuable insights and discussions.

Funding

This work was supported by the National Institutes of Health (NIH) grant MH012577 and AG085665 to BB. PAT was supported by the NIMH Intramural Research Program (ZICMH002888) of the NIH/HHS, USA.

This research was supported in part by the Intramural Research Program of the National Institutes of Health (NIH). The contributions of the NIH authors were made as part of their official duties as NIH federal employees, are in compliance with agency policy requirements, and are considered Works of the United States Government. However, the findings and conclusions presented in this paper are those of the author(s) and do not necessarily reflect the views of the NIH or the U.S. Department of Health and Human Services.

References

Biswal, B., Zerrin Yetkin, F., Haughton, V.M. and Hyde, J.S. (1995). Functional connectivity in the motor cortex of resting human brain using echo-planar mri. Magn. Reson. Med., 34: 537-541. https://doi.org/10.1002/mrm.1910340409

Biswal, B. B., & Uddin, L. Q. (2025). The history and future of resting-state functional magnetic resonance imaging. *Nature*, *641*(8065), 1121–1131. https://doi.org/10.1038/s41586-025-08953-9

Betzel, R. F., Byrge, L., He, Y., Goñi, J., Zuo, X.-N., & Sporns, O. (2014). Changes in structural and functional connectivity among resting-state networks across the human lifespan. *NeuroImage*, *102*, 345–357. https://doi.org/10.1016/j.neuroimage.2014.07.067

Black, S. E. (2007). Imaging white matter and the burden of small vessel disease. *Brain and Cognition*, *63*(2), 192-193.

Das, S.K., Hanna, G.B., Sun, H., & Biswal, B. (2025). Aberrant white matter and subcortical gray matter functional network connectivity associated with static and dynamic characteristics in subjects with temporal lobe epilepsy. Front. Neurosci. 19:1571682. doi: 10.3389/fnins.2025.1571682

Ding, Z., Huang, Y., Bailey, S. K., Gao, Y., Cutting, L. E., Rogers, B. P., Newton, A. T., & Gore, J. C. (2018). Detection of synchronous brain activity in white matter tracts at rest and under functional loading. PNAS, 115(3), 595–600.

Ding, Z., Xu, L., Gao, Y., Zhao, Y., Tan, Y., Anderson, A. W., Li, M., & Gore, J. C. (2025). Cortical modulation of resting state BOLD signals in white matter. *Scientific Reports*, *15*(1), 30056. https://doi.org/10.1038/s41598-025-14352-x

Fotiadis, P., Cieslak, M., He, X., Caciagli, L., Ouellet, M., Satterthwaite, T. D., Shinohara, R. T., & Bassett, D. S. (2023). Myelination and excitation-inhibition balance synergistically shape structure-function coupling across the human cortex. Nature Communications, 14, 6115.

Fotiadis, P., Parkes, L., Davis, K. A., Satterthwaite, T. D., Shinohara, R. T., & Bassett, D. S. (2024). Structure-function coupling in macroscale human brain networks. *Nature Reviews Neuroscience*, *25*(10), 688–704. https://doi.org/10.1038/s41583-024-00846-6

Gao, Y., Sengupta, A., Li, M., Zu, Z., Rogers, B. P., Anderson, A. W., Ding, Z., Gore, J. C., & Initiative, for the A. D. N. (2020). Functional connectivity of white matter as a biomarker of cognitive decline in Alzheimer's disease. *PLOS ONE*, *15*(10), e0240513. https://doi.org/10.1371/journal.pone.0240513

Gawryluk, J. R., D'arcy, R. C., Mazerolle, E. L., Brewer, K. D., & Beyea, S. D. (2011a). Functional mapping in the corpus callosum: A 4 T fMRI study of white matter. *Neuroimage*, *54*(1), 10-15.

Gawryluk, J. R., Mazerolle, E. L., Brewer, K. D., Beyea, S. D., & D'Arcy, R. C. (2011b). Investigation of fMRI activation in the internal capsule. *BMC neuroscience*, *12*, 56. https://doi.org/10.1186/1471-2202-12-56

Gawryluk, J. R., Mazerolle, E. L., Beyea, S. D., & D'Arcy, R. C. (2014). Functional MRI activation in white matter during the Symbol Digit Modalities Test. *Frontiers in human neuroscience*, *8*, 589.

Glasser, M. F., Sotiropoulos, S. N., Wilson, J. A., Coalson, T. S., Fischl, B., Andersson, J. L., Xu, J., Jbabdi, S., Webster, M., Polimeni, J. R., Van Essen, D. C., & Jenkinson, M. (2013). The minimal preprocessing pipelines for the Human Connectome Project. *NeuroImage, Mapping the Connectome*, *80*, 105–124. https://doi.org/10.1016/j.neuroimage.2013.04.127

Gore, J. C., Li, M., Gao, Y., Wu, T.-L., Schilling, K. G., Huang, Y., Mishra, A., Newton, A. T., Rogers, B. P., Chen, L. M., Anderson, A. W., & Ding, Z. (2019). Functional MRI and resting state connectivity in white matter—A mini-review. *Magnetic Resonance Imaging*, *63*, 1–11. https://doi.org/10.1016/j.mri.2019.07.017

Gore, J. C., Li, M., Schilling, K. G., Xu, L., Li, Y., Zu, Z., Anderson, A. W., Ding, Z., Gao, Y. (2025). The nature and interpretation of BOLD signals in white matter - A review. *Magnetic Resonance Imaging*, 127, 110596.

Grajauskas, L. A., Frizzell, T., Song, X., & D'Arcy, R. C. N. (2019). White Matter fMRI Activation Cannot Be Treated as a Nuisance Regressor: Overcoming a Historical Blind Spot. *Frontiers in Neuroscience*, *13*, 1024. https://doi.org/10.3389/fnins.2019.01024

Griffanti, L., Salimi-Khorshidi, G., Beckmann, C. F., Auerbach, E. J., Douaud, G., Sexton, C. E., Zsoldos, E., Ebmeier, K. P., Filippini, N., Mackay, C. E., Moeller, S., Xu, J., Yacoub, E., Baselli, G., Ugurbil, K., Miller, K. L., & Smith, S. M. (2014). ICA-based artefact removal and accelerated fMRI acquisition for improved resting state network imaging. *NeuroImage*, *95*, 232–247. https://doi.org/10.1016/j.neuroimage.2014.03.034

Gulban, O. F., Stirnberg, R., Tse, D. H. Y., Pizzuti, A., Koiso, K., Archila-Melendez, M. E., Huber, L. R., Bollmann, S., Goebel, R., Kay, K., & Ivanov, D. (2026). Whole-brain meso-vein imaging in living humans using fast 7-T MRI. *Science advances*, *12*(2), eaea4540. https://doi.org/10.1126/sciadv.aea4540

Guo, B., Zhou, F., Li, M., Gore, J. C., & Ding, Z. (2022). Correlated functional connectivity and glucose metabolism in brain white matter revealed by simultaneous MRI/positron emission tomography. Magnetic Resonance in Medicine, 87(3), 1507–1514.

Harris, J. J., & Attwell, D. (2012). The energetics of CNS white matter. Journal of Neuroscience, 32(1), 356–371.

Huang, Y., Glasier, C. M., Na, X., & Ou, X. (2024). White matter functional networks in the developing brain. *Frontiers in Neuroscience*, *18*. https://doi.org/10.3389/fnins.2024.1467446

Huang, Y., Wei, P.-H., Xu, L., Chen, D., Yang, Y., Song, W., Yi, Y., Jia, X., Wu, G., Fan, Q., Cui, Z., & Zhao, G. (2023). Intracranial electrophysiological and structural basis of BOLD functional connectivity in human brain white matter. *Nature Communications*, *14*(1), 3414. https://doi.org/10.1038/s41467-023-39067-3

Itkyal, V. S., Iraji, A., Jensen, K. M., LaGrow, T. J., Duda, M., Turner, J. A., Liu, A., Wu, L., Du, Y., Fries, J., Fu, Z., Kochunov, P., Belger, A., Ford, J. M., Mathalon, D. H., Pearlson, G. D., Potkin, S. G., Preda, A., van Erp, T. G. M., Yang, K., Sawa, A., Hutchison, K., Osuch, E. A., Theberge, J., Abbott, C. Mueller, B. A., Chen, J., Sui, J., Adali, T., & Calhoun, V. D. (2025). Evidence for white matter intrinsic connectivity networks at rest and during a task: a large-scale study and templates. *Network Neuroscience*, *9*(4), 1221-1244.

Jain, P., Michael, A. M., Wang, P., Di, X., & Biswal, B. (2025). WhiFuN: A toolbox to map the white matter functional networks of the human brain. *Imaging Neuroscience*, *3*, IMAG.a.3. https://doi.org/10.1162/IMAG.a.3

Jeurissen, B., Leemans, A., Tournier, J. D., Jones, D. K., & Sijbers, J. (2013). Investigating the prevalence of complex fiber configurations in white matter tissue with diffusion magnetic resonance imaging. Human Brain Mapping, 34(11), 2747–2766.

Jeurissen, B., Tournier, J.-D., Dhollander, T., Connelly, A., & Sijbers, J. (2014). Multi-tissue constrained spherical deconvolution for improved analysis of multi-shell diffusion MRI data. *NeuroImage*, *103*, 411–426. https://doi.org/10.1016/j.neuroimage.2014.07.061

Jiang, J., Kang, T., Ling, R., Liu, Y., Sun, J., Li, Y., Li, X., Yang, H., Huang, B., & the Alzheimer's Disease Neuroimaging Initiative. (2025). Uncovering abnormal gray and white matter connectivity patterns in Alzheimer's disease spectrum: A dynamic graph theory analysis for early detection. *Frontiers in Aging Neuroscience*, *17*. https://doi.org/10.3389/fnagi.2025.1589018

Kelly, S., Jahanshad, N., Zalesky, A., Kochunov, P., Agartz, I., Alloza, C., Andreassen, O. A., Arango, C., Banaj, N., Bouix, S., Bousman, C. A., Brouwer, R. M., Bruggemann, J., Bustillo, J., Cahn, W., Calhoun, V., Cannon, D., Carr, V., Catts, S., … Donohoe, G. (2018). Widespread white matter microstructural differences in schizophrenia across 4322 individuals: Results from the ENIGMA Schizophrenia DTI Working Group. *Molecular Psychiatry*, *23*(5), 1261–1269. https://doi.org/10.1038/mp.2017.170

Kinnunen, K. M., Greenwood, R., Powell, J. H., Leech, R., Hawkins, P. C., Bonnelle, V., Patel, M. C., Counsell, S. J., & Sharp, D. J. (2011). White matter damage and cognitive impairment after traumatic brain injury. *Brain*, *134*(2), 449–463. https://doi.org/10.1093/brain/awq347

Li, J., Chen, H., & Liao, W. (2025). Mapping the white-matter functional connectome: A personal perspective. *Psychoradiology*, *5*, kkaf028. https://doi.org/10.1093/psyrad/kkaf028

Li, M., Newton, A. T., Anderson, A. W., Ding, Z., & Gore, J. C. (2019). Characterization of the hemodynamic response function in white matter tracts for event-related fMRI. *Nature Communications*, *10*(1), 1140. https://doi.org/10.1038/s41467-019-09076-2

Li, M., Schilling, K. G., Xu, L., Choi, S., Gao, Y., Zu, Z., Anderson, A. W., Ding, Z., & Gore, J. C. (2024). White matter engagement in brain networks assessed by integration of functional and structural connectivity. *NeuroImage*, *302*, 120887. https://doi.org/10.1016/j.neuroimage.2024.120887

Logothetis, N. K., Pauls, J., Augath, M., Trinath, T., & Oeltermann, A. (2001). Neurophysiological investigation of the basis of the fMRI signal. *nature*, *412*(6843), 150-157.

Looser, Z. J., Faik, Z., Ravotto, L., Zanker, H. S., Jung, R. B., Werner, H. B., Ruhwedel, T., Möbius, W., Bergles, D. E., Barros, L. F., Nave, K.-A., Weber, B., & Saab, A. S. (2024). Oligodendrocyte–axon metabolic coupling is mediated by extracellular K+ and maintains axonal health. *Nature Neuroscience*, *27*(3), 433–448. https://doi.org/10.1038/s41593-023-01558-3

Marussich, L., Lu, K.-H., Wen, H., & Liu, Z. (2017). Mapping White-Matter Functional Organization at Rest and during Naturalistic Visual Perception. *NeuroImage*, *146*, 1128–1141. https://doi.org/10.1016/j.neuroimage.2016.10.005

Nelson, M. C., Da Lu, W., Leppert, I. R., Hansen, H. A., Rowley, C. D., Misic, B., & Tardif, C. L. (2026). The role of white matter myelin in structural-functional network coupling. *Communications Biology*, *9*(1), 488. https://doi.org/10.1038/s42003-026-09813-6

Noble, S., Scheinost, D., & Constable, R. T. (2019). A decade of test-retest reliability of functional connectivity: A systematic review and meta-analysis. *NeuroImage*, *203*, 116157. https://doi.org/10.1016/j.neuroimage.2019.116157

Özbay, P. S., Chang, C., Picchioni, D., Mandelkow, H., Moehlman, T. M., Chappel-Farley, M. G., van Gelderen, P., de Zwart, J. A., & Duyn, J. H. (2018). Contribution of systemic vascular effects to fMRI activity in white matter. *NeuroImage*, *176*, 541–549. https://doi.org/10.1016/j.neuroimage.2018.04.045

Peer, M., Nitzan, M., Bick, A. S., Levin, N., & Arzy, S. (2017). Evidence for Functional Networks within the Human Brain's White Matter. *The Journal of Neuroscience: The Official Journal of the Society for Neuroscience*, *37*(27), 6394–6407. https://doi.org/10.1523/JNEUROSCI.3872-16.2017

Penke, L., Maniega, S. M., Murray, C., Gow, A. J., Hernández, M. C. V., Clayden, J. D., Starr, J. M., Wardlaw, J. M., Bastin, M. E., & Deary, I. J. (2010). A General Factor of Brain White Matter Integrity Predicts Information Processing Speed in Healthy Older People. *Journal of Neuroscience*, *30*(22), 7569–7574. https://doi.org/10.1523/JNEUROSCI.1553-10.2010

Preti, M. G., & Van De Ville, D. (2019). Decoupling of brain function from structure reveals regional behavioral specialization in humans. *Nature Communications*, *10*(1), 4747. https://doi.org/10.1038/s41467-019-12765-7

Saab, A. S., Tzvetavona, I. D., Trevisiol, A., Baltan, S., Dibaj, P., Kusch, K., Möbius, W., Goetze, B., Jahn, H. M., Huang, W., Steffens, H., Schomburg, E. D., Pérez-Samartín, A., Pérez-Cerdá, F., Bakhtiari, D., Matute, C., Löwel, S., Griesinger, C., Hirrlinger, J., Kirchhoff, F., & Nave, K. A. (2016). Oligodendroglial NMDA Receptors Regulate Glucose Import and Axonal Energy Metabolism. *Neuron*, *91*(1), 119–132. https://doi.org/10.1016/j.neuron.2016.05.016

Salimi-Khorshidi, G., Douaud, G., Beckmann, C. F., Glasser, M. F., Griffanti, L., & Smith, S. M. (2014). Automatic denoising of functional MRI data: Combining independent component analysis and hierarchical fusion of classifiers. *NeuroImage*, *90*, 449–468. https://doi.org/10.1016/j.neuroimage.2013.11.046

Schilling, K. G., Gao, Y., Li, M., Wu, T.-L., Blaber, J., Landman, B. A., Anderson, A. W., Ding, Z., & Gore, J. C. (2019). Functional tractography of white matter by high angular resolution functional-correlation imaging (HARFI). *Magnetic Resonance in Medicine*, *81*(3), 2011–2024. https://doi.org/10.1002/mrm.27512

Schilling, K. G., Li, M., Rheault, F., Gao, Y., Cai, L., Zhao, Y., Xu, L., Ding, Z., Anderson, A. W., Landman, B. A., & Gore, J. C. (2023). Whole-brain, gray, and white matter time-locked functional signal changes with simple tasks and model-free analysis. *Proceedings of the National Academy of Sciences*, *120*(42), e2219666120. https://doi.org/10.1073/pnas.2219666120

Seguin, C., Sporns, O., & Zalesky, A. (2023). Brain network communication: Concepts, models and applications. *Nature Reviews Neuroscience*, *24*(9), 557–574. https://doi.org/10.1038/s41583-023-00718-5

Smith, R. E., Tournier, J.-D., Calamante, F., & Connelly, A. (2012). Anatomically constrained tractography: Improved diffusion MRI streamlines tractography through effective use of anatomical information. *NeuroImage*, *62*(3), 1924–1938. https://doi.org/10.1016/j.neuroimage.2012.06.005

Tournier, J.-D. (2019). Diffusion MRI in the brain – Theory and concepts. *Progress in Nuclear Magnetic Resonance Spectroscopy*, *112–113*, 1–16. https://doi.org/10.1016/j.pnmrs.2019.03.001

Tournier, J.-D., Smith, R., Raffelt, D., Tabbara, R., Dhollander, T., Pietsch, M., Christiaens, D., Jeurissen, B., Yeh, C.-H., & Connelly, A. (2019). *MRtrix3*: A fast, flexible and open software framework for medical image processing and visualisation. *NeuroImage*, *202*, 116137. https://doi.org/10.1016/j.neuroimage.2019.116137

Van Essen, D. C., Smith, S. M., Barch, D. M., Behrens, T. E. J., Yacoub, E., & Ugurbil, K. (2013). The WU-Minn Human Connectome Project: An overview. *NeuroImage, Mapping the Connectome*, *80*, 62–79. https://doi.org/10.1016/j.neuroimage.2013.05.041

Vázquez-Rodríguez, B., Suárez, L. E., Markello, R. D., Shafiei, G., Paquola, C., Hagmann, P., van den Heuvel, M. P., Bernhardt, B. C., Spreng, R. N., & Misic, B. (2019). Gradients of structure–function tethering across neocortex. *Proceedings of the National Academy of Sciences*, *116*(42), 21219–21227. https://doi.org/10.1073/pnas.1903403116

Veraart, J., Novikov, D. S., Christiaens, D., Ades-aron, B., Sijbers, J., & Fieremans, E. (2016). Denoising of diffusion MRI using random matrix theory. *NeuroImage*, *142*, 394–406. https://doi.org/10.1016/j.neuroimage.2016.08.016

Wang, H., Wang, X., Wang, Y., Zhang, D., Yang, Y., Zhou, Y., Qui, B., & Zhang, P. (2023). White matter BOLD signals at 7 Tesla reveal visual field maps in optic radiation and vertical occipital fasciculus. *NeuroImage*, *269*, 119916.

Wang, P., Wang, J., Tang, Q., Alvarez, T. L., Wang, Z., Kung, Y. C., Lin, C. P., Chen, H., Meng, C., & Biswal, B. B. (2021). Structural and functional connectivity mapping of the human corpus callosum organization with white-matter functional networks. *NeuroImage*, *227*, 117642. https://doi.org/10.1016/j.neuroimage.2020.117642

Wang, P., Wang, J., Michael, A., Wang, Z., Klugah-Brown, B., Meng, C., & Biswal, B. B. (2022). White Matter Functional Connectivity in Resting-State fMRI: Robustness, Reliability, and Relationships to Gray Matter. *Cerebral Cortex*, *32*(8), 1547–1559. https://doi.org/10.1093/cercor/bhab181

Zhao, J., Huang, C.-C., Zhang, Y., Liu, Y., Tsai, S.-J., Lin, C.-P., & Lo, C.-Y. Z. (2023). Structure-function coupling in white matter uncovers the abnormal brain connectivity in Schizophrenia. *Translational Psychiatry*, *13*(1), 214. https://doi.org/10.1038/s41398-023-02520-4

Zhou, X., Zhang, X., Wang, P., Chen, H., Liao, W., & Biswal, B. B. (2023). Spatiotemporal topological correspondence between blood oxygenation and glucose metabolism revealed by simultaneous fPET-fMRI in brain's white matter. Cerebral Cortex, 33(15), 9291–9302.

Zu, Z., Choi, S., Zhao, Y., Gao, Y., Li, M., Schilling, K. G., Ding, Z., & Gore, J. C. (2024). The missing third dimension: Functional correlations of BOLD signals incorporating white matter. *Science Advances*, *10*(4), eadi0616. https://doi.org/10.1126/sciadv.adi0616

Supplementary Files

This is a list of supplementary files associated with this preprint. Click to download.

- SupplementaryMaterialWMSCFC.docx